

LFMamba: Light Field Image Super-Resolution with State Space Model

Wang Xia, *Student Member, IEEE*, Yao Lu, *Member, IEEE*, Shunzhou Wang, *Member, IEEE*, Ziqi Wang, Peiqi Xia, and Tianfei Zhou

Abstract—Recent years have witnessed significant advancements in light field image super-resolution (LFSR) owing to the progress of modern neural networks. However, these methods often face challenges in capturing long-range dependencies (CNN-based) or encounter quadratic computational complexities (Transformer-based), which limit their performance. Recently, the State Space Model (SSM) with selective scanning mechanism (S6), exemplified by Mamba, has emerged as a superior alternative in various vision tasks compared to traditional CNN- and Transformer-based approaches, benefiting from its effective long-range sequence modeling capability and linear-time complexity. Therefore, integrating S6 into LFSR becomes compelling, especially considering the vast data volume of 4D light fields. However, the primary challenge lies in *designing an appropriate scanning method for 4D light fields that effectively models light field features*. To tackle this, we employ SSMs on the informative 2D slices of 4D LFs to fully explore spatial contextual information, complementary angular information, and structure information. To achieve this, we carefully devise a basic SSM block characterized by an efficient SS2D mechanism that facilitates more effective and efficient feature learning on these 2D slices. Based on the above two designs, we further introduce an SSM-based network for LFSR termed LFMamba. Experimental results on LF benchmarks demonstrate the superior performance of LFMamba. Furthermore, extensive ablation studies are conducted to validate the efficacy and generalization ability of our proposed method. We expect that our LFMamba shed light on effective representation learning of LFs with state space models.

Index Terms—Light Field, Image Super-Resolution, State Space Model, Mamba.

I. INTRODUCTION

LIGHT field (LF) cameras record both the intensity and direction of light rays emitted from the world, enabling a wide range of valuable applications such as depth estimation [1], refocusing [2], and salience detection [3]. However, LF images captured by these cameras often sacrifice spatial resolution in individual sub-aperture images (SAIs) to capture

multiple viewpoints simultaneously, limiting their usability in certain applications. Hence, there arises a necessity to enhance the spatial resolution of LF images, a task known as light field image super-resolution (LFSR).

Taking advantage of CNNs, Yoon et al. [4] made the first attempt to employ SRCNN [5] to achieve LFSR and light field image angular super-resolution (LFASR). Specifically, they first utilize SRCNN to enhance the resolution of each SAI, and then, adjacent HR SAIs are combined for novel view synthesis to increase the angular resolution by another SRCNN. Despite significant improvements over traditional methods [6–10], super-resolving each SAI individually remains suboptimal, as it overlooks the rich angular information available across different SAIs. Subsequently, a series of more sophisticated networks have been proposed to fully exploit the abundant spatial-angular information inherent in light fields, further enhancing the reconstruction accuracy [11–21]. Despite the progress they have achieved, the natural local reductive bias of convolutions limits the exploration of non-local relations of LFs. Additionally, the static learned kernel weights render these networks inflexible for out-of-distribution input light fields with various unseen scenarios.

Transformer [22], initially introduced in the field of natural language processing, has proven effective in modeling long-range dependencies and dynamically adjusting weights according to inputs. Consequently, it has found widespread application in various vision tasks, such as image classification [23, 24], object detection [25, 26], semantic segmentation [27, 28], and image restoration [29, 30], becoming the de facto dominant architecture in vision areas. In recent years, a plethora of Transformer-based methods have been proposed to tackle LFSR [31–36]. These methods commonly leverage the self-attention mechanism to establish long-range interrelationships from different views [31, 33, 34] or specific LF subspace domains [32, 35, 36], enabling effective excavation of global features and thereby further enhancing the reconstruction quality. However, the quadratic computational complexity of self-attention calculation hinders their efficient and comprehensive exploration of intrinsic properties in LFs.

Recently, the State Space Models (SSMs) [37–41] have emerged as a novel and promising class of foundational architectures for sequence modeling. Among these, Mamba [41], a type of SSM endowed with selective mechanism (S6) that grants it content-based reasoning abilities, stands out by outperforming Transformer across various modalities including language, audio, and genomics in performance and efficiency. Inspired by these advancements, accompanying

This work was supported in part by the Special Projects in key areas of Guangdong Province (No.2022ZDZX1036), and in part by Shenzhen Peacock Plan. *Corresponding author: Yao Lu* (vis_y1@smbu.edu.cn)

Wang Xia, Yao Lu, Ziqi Wang, Peiqi Xia, and Tianfei Zhou are with School of Computer, Beijing Institute of Technology, Beijing 100081, China (e-mail: wangxia@bit.edu.cn; vis_y1@smbu.edu.cn; {3220221026, 3120221009, tfzhou}@bit.edu.cn).

Yao Lu and Wang Xia are also with Guangdong Laboratory of Machine Perception and Intelligent Computing, Department of Engineering, Shenzhen MSU-BIT University, Shenzhen 518172, China.

Shunzhou Wang is with School of Electronic and Computer Engineering, Shenzhen Graduate School, Peking University, Shenzhen 518055, China. (email: shunzhouwang@163.com).

Codes are public available at <https://github.com/stanley-313/LFMamba>.

Manuscript received xxx, 2024; revised xxx, 2024.

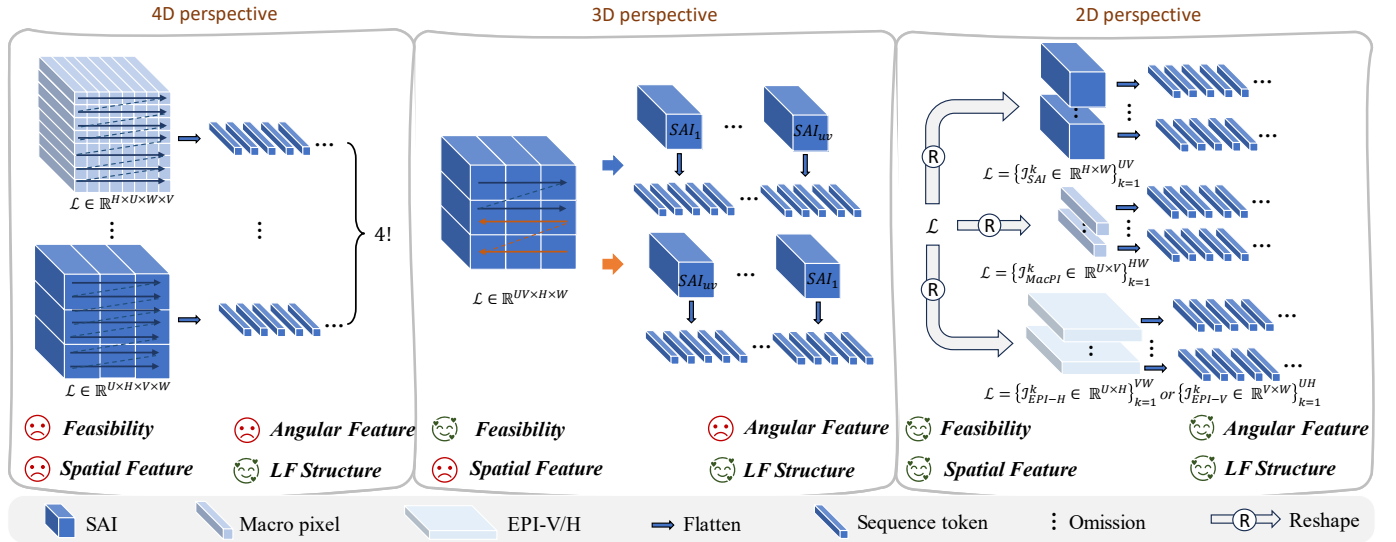


Fig. 1. **Three different perspectives to model LFs using State Space Model.** The key point is how to flatten a 4D LF into a 1D sequence. *Left:* Taking the 4D LF data as a whole and flatten it by different orders. *Mid:* Taking LF as an 3D image sequence to explore the relationships between sub-aperture images. *Right:* Taking LF as a combination of informative 2D data slices (i.e., sub-aperture image (SAI), macro-pixel image (MacPI), and epipolar plane image (EPI)) to fully capture spatial contextual information, complementary angular information, and structure information.

research has focused on exploring the potential of Mamba in vision tasks [42–49], demonstrating the feasibility and superiority of Mamba in vision fields.

Naturally, a question arises: how can we integrate Mamba into LFSR effectively? To answer that, we should first recognize the prominent challenge is *designing an appropriate way to scan 4D LFs that can fully explore the useful information of LFs*, considering the high dimensionality and complexity of LF data. To solve this problem, we initially devised three probable solutions from different perspectives as shown in Fig. 1. The first, and perhaps the most straightforward idea is to flatten the 4D light field into a 1D sequence by different orders. However, given a total of $4! = 24$ permutations, exhaustively searching the entire order space to ensure comprehensive modeling of the LFs is infeasible, and since the spatial and angular tokens are highly intertwined, the spatial contextual and angular information may be difficult to explore. The second viewpoint is to regard LFs as a 3D image sequence and flatten them by order as done in [45] to explore the relationships of the image sequence. While this may uncover structural information considering the discrepancies between adjacent view images, it may also underutilize fundamental spatial contextual and angular information that is embedded in entire sequences. Lastly, drawing inspiration from visual state space models [43, 47], we can adopt Mamba to informative 2D slices (i.e., sub-aperture image (SAI), macro-pixel image (MacPI), and epipolar plane image (EPI)) of 4D LFs to independently extract spatial, angular, and EPI features, which is more effective and easier for implementation.

Based on the above analysis, we introduce LFMamba, a novel SSM-based network for LFSR. Specifically, to achieve effective feature extraction on LFs’ 2D slices, we first carefully devise a basic SSM block which is the core component of LFMamba. The basic SSM block integrates the proposed

efficient SS2D, significantly reducing parameters with minimal performance drop. By utilizing the basic SSM block on LFs’ 2D informative slices, LFMamba achieves a thorough exploration of diverse LF features. In summary, our contributions are as follows:

- We integrate the State Space Model (SSM) into LFSR for the first time by adopting SSM on LFs’ 2D informative slices, which facilitates effective and comprehensive exploration of LFs’ spatial contextual information, complementary angular information, and structure information.
- We design a basic SSM block featuring the proposed efficient SS2D mechanism. As the fundamental feature extractor of LF’s 2D slices, it significantly reduces the parameters with little expressivity loss.
- We propose an SSM-based network LFMamba for LFSR. Experimental results on LF benchmarks show LFMamba’s efficacy and efficiency compared to state-of-the-art methods. We further demonstrate our method’s generalization ability by applying LFMamba for LF angular SR task.

II. RELATED WORK

A. Light Field Image Super-Resolution

Light field image super-resolution (LFSR), aiming at enhancing the spatial resolution of each SAI, has generated widespread attention in recent years. Since Yoon et al. [4] first introduced CNNs into this realm, numerous learning-based methods have been proposed, showcasing progressive performance improvements. Inspired by LFCNN [4], Yuan et al. [50] employed a more powerful single image super-resolution (SISR) network EDSR [51] to increase the spatial resolution of SAIs, followed by another EPI-enhancement network to refine the results. After that, several multi-stream

networks were proposed to exploit relationships between different SAIs. Wang et al. [11] designed two bidirectional recurrent networks to iteratively model spatial relations between horizontal and vertical SAIs. Zhang et al. [12, 15] introduced a multi-branch network to learn the sub-pixel shift information of stacked SAIs in four directions. Jin et al. [14] proposed an all-to-one approach implemented by a weight-shared multi-stream network, which combined all views for complementary information extraction and utilization. Apart from these methods, Yeung et al. [13] proposed spatial-angular separable convolution (SAS-Conv) to approximate 4D convolution while achieving efficiency. Wang et al. [17] and Liu et al. [19] proposed LF-InterNet and IINet, wherein both the spatial and angular features were extracted interactively. Wang et al. [16] utilized deformable convolution to align the spatial feature to the center view, addressing the disparity problem. More recently, Cheng et al. [20] combined spatial-angular correlated convolution with SAS-Conv and proposed spatial-angular versatile convolution. Wang et al. [18] proposed a generic LF disentangling mechanism for LFSR, LF angular super-resolution, and depth estimation. Van Duong et al. [21] further completed [18] by considering the inter-spatial and inter-angular relations.

Despite the intricate designs and architectures, performance reaches a bottleneck as these methods rely on convolution layers, which face crucial challenges in exploiting non-local spatial-angular information due to the limited receptive field capabilities. In response, some researchers have resorted to Transformer architectures, leveraging their robust long-range dependency modeling capabilities to break through this ceiling. Wang et al. [31] proposed a two-branch network, which established long-range dependencies along horizontal and vertical SAI sequences. Wang et al. [33] proposed a local-global aggregation network by combining CNNs and Transformer. Following the SAS-Conv scheme [13], Liang et al. [32] replaced convolutions with Transformer layers, resulting in superior performance. Wang and Lu [34] employed Transformer to learn multi-granularity relationships between SAIs. Liang et al. [36] proposed EPIT which adopted Transformer to learn non-local spatial-angular correlation on EPI, achieving state-of-the-art performance. Despite the promising results, the quadratic computational complexity and memory footprint pose significant challenges for achieving efficient and effective LFSR. Notably, Cong et al. [35] proposed a sub-sampled spatial Transformer inspired by PVT [52] to reduce the computational overhead. However, the improvement is limited and the computational complexity remains quadratic. More advanced sub-quadratic complexity attention mechanisms (e.g., swin [24], linear attention [53], flash attention [54]) or recent state space models (SSMs) [37, 40, 41] with linear complexity, are desired in this field.

B. State Space Model

State Space Models (SSMs) [37–39], originating from classic control theory, have recently emerged as competitive backbones for state space transformation in deep learning. Their notable property of linearly scaling with sequence length

in long-range dependency modeling has garnered significant interest from researchers. For instance, the structured state-space sequence model (S4) [37] is a pioneering work in deep state-space modeling for long-range dependency. Subsequently, the S5 layer [38] was proposed, building upon S4 and introducing MIMO (Multiple Input Multiple Output) and efficient parallel scanning. Additionally, H3 [40] has achieved promising results, narrowing the performance gap between SSMS and Transformers in natural language processing. Mehta et al. [55] integrate gated units into S4, further advancing the improvement of S4, and leading to the development of the gated state space layer. S4nd [56] is the pioneer in extending the applicability of SSMS beyond sequential data to continuous data domains such as images and videos, bridging the gap between sequential and spatial modeling. More recently, Mamba [41], a data-dependent SSM with a selective mechanism (S6) and efficient hardware design, has surpassed Transformers in natural language processing tasks while demonstrating linear scaling with input length. Subsequently, numerous works have introduced Mamba into various vision tasks, including image classification [42, 43, 49], biomedical image segmentation [44, 45, 57], and image restoration [46–48], and achieve comparable or superior performance in terms of accuracy and efficiency.

III. METHOD

In this section, we start with an introduction to the state space model for light fields (Section. III-A). Then, we elaborate on the overall architecture of LFMamba in Section. III-B. After that, we expound on the process of how LFMamba learns spatial-angular features (Section. III-C) and structure features (Section. III-D) by our proposed basic SSM blocks. Then, we give a detailed introduction to the basic SSM block in Section. III-E. At last, in Section. III-F, we summarize the overall algorithm for achieving LFSR using LFMamba.

A. State Space Model for Light Field

State Space Models (SSMs) are a type of linear time-invariant systems that map 1-D continuous simulation $x(t) \in \mathbb{R}^N$ into response $y(t) \in \mathbb{R}^N$, which the process can be formulated by linear ordinary differential equations (ODEs)

$$\begin{aligned} h'(t) &= \mathbf{A}h(t) + \mathbf{B}x(t), \\ y(t) &= \mathbf{C}h(t), \end{aligned} \quad (1)$$

where the output $y(t)$ is derived from the input signal $x(t)$ and hidden state $h(t) \in \mathbb{R}^N$, and the parameters of the system include a state transition matrix $\mathbf{A} \in \mathbb{R}^{N \times N}$, and projection matrices $\mathbf{B} \in \mathbb{R}^N$ and $\mathbf{C} \in \mathbb{R}^N$. To integrate SSM into deep learning, a discretization process on ODEs is required, where in S4 [37], \mathbf{A} and \mathbf{B} are discretized by zero-order hold (ZOH) to generate discrete parameters $\bar{\mathbf{A}}$ and $\bar{\mathbf{B}}$ using a time scale parameter Δ

$$\begin{aligned} \bar{\mathbf{A}} &= \exp(\Delta\mathbf{A}), \\ \bar{\mathbf{B}} &= (\Delta\mathbf{A})^{-1}(\exp(\Delta\mathbf{A}) - \mathbf{I}) \cdot \Delta\mathbf{B}, \end{aligned} \quad (2)$$

After discretization, the discrete version of Eq. (1) can be rewritten as,

$$\begin{aligned} h_k &= \bar{\mathbf{A}}h_{k-1} + \bar{\mathbf{B}}x_k, \\ y_k &= \mathbf{C}h_k, \end{aligned} \quad (3)$$

At last, the output can be calculated in a global convolution form, enabling efficient parallelizable training.

$$\begin{aligned} \bar{\mathbf{K}} &= (\mathbf{C}\bar{\mathbf{B}}, \mathbf{C}\bar{\mathbf{A}}\bar{\mathbf{B}}, \dots, \mathbf{C}\bar{\mathbf{A}}^{L-1}\bar{\mathbf{B}}), \\ y &= x * \bar{\mathbf{K}} \end{aligned} \quad (4)$$

where L is the length of the input sequence, and $\bar{\mathbf{K}} \in \mathbb{R}^L$ denotes the structured convolutional kernel.

So far, the discretization of SSM facilitates efficient training while limited in content awareness compression due to its data-independent and time-invariant properties. Consequently, selective SSM (Mamba or S6) [41] introduce data-dependent parameters ($\mathbf{B}, \mathbf{C}, \mathbf{\Delta}$) derived from the input data x through a simple linear projection layer, ensuring its awareness of the contextual information embedded in the input data.

The 4D LF is parameterized by the two-plane model [58] as $\mathcal{L}(u, v, h, w) \in \mathbb{R}^{U \times V \times H \times W}$, where $U \times V$ represent the angular resolution, and $H \times W$ represent the spatial resolution. To apply SSM or Mamba to LFs, we regard 4D LF as combinations of four informative 2D slices $\mathcal{L} = \{\mathcal{L}_{SAI}, \mathcal{L}_{MacPI}, \mathcal{L}_{EPI-H}, \mathcal{L}_{EPI-V}\}$ as introduced in Fig. 1, where

$$\begin{aligned} \mathcal{L}_{SAI}(:, :, h, w) &= \{\mathcal{I}_{SAI}^i \in \mathbb{R}^{H \times W}\}_{i=1}^{UV}, \\ \mathcal{L}_{MacPI}(u, v, :, :) &= \{\mathcal{I}_{MacPI}^i \in \mathbb{R}^{U \times V}\}_{i=1}^{HW}, \\ \mathcal{L}_{EPI-H}(u, :, h, :) &= \{\mathcal{I}_{EPI-H}^i \in \mathbb{R}^{H \times U}\}_{i=1}^{WV}, \\ \mathcal{L}_{EPI-V}(:, v, :, w) &= \{\mathcal{I}_{EPI-V}^i \in \mathbb{R}^{W \times V}\}_{i=1}^{HU} \end{aligned} \quad (5)$$

Then, each 2D LF slice can be projected into the high-dimensional space and be flattened to generate a 1D sequence, which serves as the input for the SSM system. Taken \mathcal{L}_{SAI} as an example, we first project it to produce a high-dimensional feature $\mathbf{L}_{SAI} = \{\mathbf{I}_{SAI}^i \in \mathbb{R}^{H \times W \times C}\}_{i=1}^{UV}$. Each \mathbf{I}_{SAI}^i is then reshaped into a 1D sequence of length HW as $\mathbf{T}_{SAI}^i = \{t_k^i \in \mathbb{R}^C\}_{k=1}^{HW}$. Subsequently, t_k^i can be fed into an SSM system the same as x_k in Eq. (3) to predict the corresponding output. In that way, the spatial contextual information of LFs is effectively extracted. Therefore, similar processes can be performed on \mathcal{L}_{MacPI} , \mathcal{L}_{EPI-H} , and \mathcal{L}_{EPI-V} to fully exploit the angular information and structure information of LFs.

Based on the above principle, we introduce a basic SSM block (see Section. III-E) that takes these 2D slices embedding as input. We further develop a novel SSM-based network based on this, termed LFMamba for LFSR, and we will present a detailed introduction of LFMamba in the following part.

B. Overview of LFMamba

For the problem of LFSR, given a low-resolution LF image $\mathcal{L}_{lr} \in \mathbb{R}^{U \times V \times H \times W}$, the goal of LFSR is to reconstruct the high-resolution LF image $\mathcal{L}_{hr} \in \mathbb{R}^{U \times V \times \alpha H \times \alpha W}$, where α is the upscaling factor. Following prior works [18, 32], the LF image is organized as a $U \times V$ sub-aperture images array, and we convert it to YCbCr color space and only super-resolve the Y channel.

As shown in Fig. 2(a), LFMamba mainly comprises four parts: Initial Feature Extraction module (IFE), Spatial-Angular Feature Learning module (SAFL), LF Structure Feature Learning module (LSFL), and HR LF Reconstruction module (HLFR). Specifically, following [32], the input LF images \mathcal{L}_{lr} are first processed by cascaded convolution layers to extract initial spatial features $\mathbf{F}_{init} \in \mathbb{R}^{U \times V \times H \times W \times C}$, where C denotes the channel dimension and is set to 64 in our implementation. Then, the features will be further transferred to the SAFL module to capture the spatial contextual feature and complementary angular information. After that, the middle features $\mathbf{F}_{sa} \in \mathbb{R}^{U \times V \times H \times W \times C}$ will be processed by the LSFL module to incorporate the structural information of LFs to generate $\mathbf{F}_{struct} \in \mathbb{R}^{U \times V \times H \times W \times C}$. Subsequently, we fuse the above three features via concatenation followed by a 1×1 convolution layer to achieve multi-level feature utilization.

$$\mathbf{F}_{fuse} = \text{Conv}(\text{Concat}(\mathbf{F}_{init}, \mathbf{F}_{sa}, \mathbf{F}_{struct})) \quad (6)$$

Lastly, following most precious works [18, 32, 36], the fused feature \mathbf{F}_{fuse} will undergo a pixel shuffling layer and a convolution layer to generate the final HR LF image \mathcal{L}_{hr} .

C. Spatial-Angular Feature Learning

The SAFL module endeavors to comprehensively integrate the spatial contextual information and complementary angular information inherent in LFs. To this end, we devise a spatial SSM block and an angular SSM block, and employ a simple but effective spatial-angular separable modeling scheme [13, 32], in which case, as illustrated in Fig. 2(a), the spatial SSM block and the angular SSM block are adopted alternately for three times with local skip connection.

$$\begin{aligned} \mathbf{F}_{sa} &= \text{H}_{SAFL}(\mathbf{F}_{init}) + \mathbf{F}_{init}, \\ \text{H}_{SAFL}(\cdot) &= \text{H}_{spa}^3(\text{H}_{ang}^3(\dots \text{H}_{spa}^1(\text{H}_{ang}^1(\cdot)))) \end{aligned} \quad (7)$$

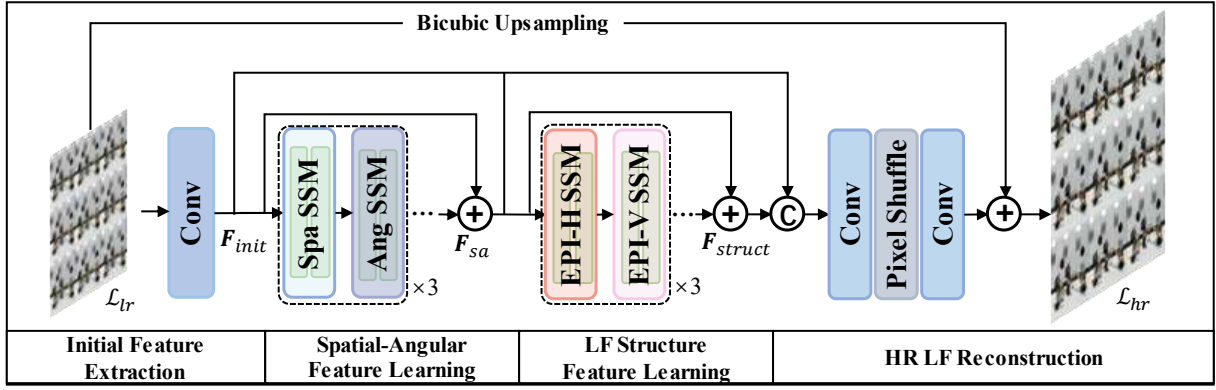
where $\text{H}_{SAFL}(\cdot)$ denotes the SAFL module, $\text{H}_{spa}(\cdot)$ and $\text{H}_{ang}(\cdot)$ represent the spatial SSM block and angular SSM block, respectively.

The spatial SSM block is designed for spatial contextual information extraction on each individual SAI. Specifically, for a given input 4D LF feature $\mathbf{F} \in \mathbb{R}^{U \times V \times H \times W \times C}$, we first reshape it to its 2D SAI form $\mathbf{F}_{SAI} \in \mathbb{R}^{UV \times H \times W \times C}$ to facilitate more effective spatial feature extraction, where UV denotes the batch size. After that, two basic SSM blocks (see Fig. 2(b) and detail introduction in Section. III-E) are adopted for spatial feature extraction. After that, the feature is reshaped back to its 4D form for further processing, which can be formulated as

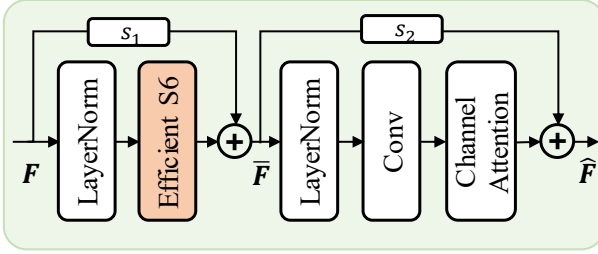
$$\begin{aligned} \mathbf{F}_{SAI} &= \text{Reshape}(\mathbf{F}), \\ \hat{\mathbf{F}}_{SAI} &= \text{H}_{SSM}^2(\text{H}_{SSM}^1(\mathbf{F}_{SAI})), \\ \hat{\mathbf{F}} &= \text{Reshape}(\hat{\mathbf{F}}_{SAI}) \end{aligned} \quad (8)$$

where $\hat{\mathbf{F}}_{SAI}$ and $\hat{\mathbf{F}}$ denotes the enhanced features, and H_{SSM} denote the basic SSM block.

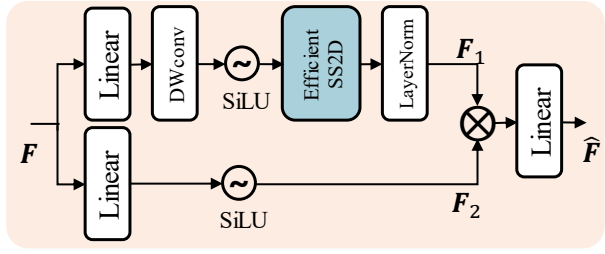
The angular SSM block adopts a similar processing approach, we reshape the input 4D LF feature to its 2D macro pixel form (i.e., $\mathbb{R}^{HW \times U \times V \times C}$) to achieve angular feature learning by another two basic SSM blocks and finally reshaped the feature back to its 4D representation.



(a) Overall architecture



(b) Basic SSM block



(c) Efficient S6

Fig. 2. **LFMamba**. (a) The overall architecture of LFMamba. (b) The detailed structure of the core component, the basic SSM block. (c) The illustration of the proposed efficient S6.

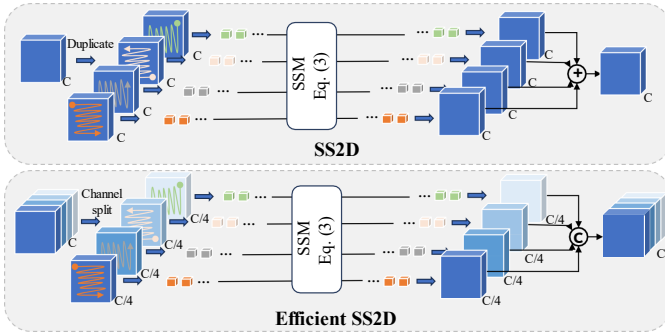


Fig. 3. **Illustration of the original SS2D and our efficient SS2D. Up:** Original SS2D in visual state sapce model [43] copies the input four times for different scanning orders. **Down:** Our proposed efficient SS2D divides the input into four groups along the channel dimension for different scanning orders, which significantly reduces the parameters with little performance decline.

D. LF Structure Feature Learning

After extracting spatial contextual and complementary angular information of LFs, further excavating the structural property of LFs is crucial for reconstructing accurate HR LF images. In the LSFL module, we empirically adopt basic SSM blocks on horizontal and vertical EPIs as they are highly correlated with the scene depth, to exploit the structure information of LFs. As depicted in Fig. 2(a), in the LFSL module, we alternately perform EPI-H and EPI-V SSM block three times to achieve LF structure learning. The EPI-H/V SSM block also follows the previous process to reshape the input LF feature to the corresponding forms

(i.e., $F_{EPI_H} \in \mathbb{R}^{VW \times U \times H \times C}$, $F_{EPI_V} \in \mathbb{R}^{UH \times V \times W \times C}$) before being fed into the basic SSM blocks. Similar to [36], we share the parameters between horizontal and vertical EPI SSM blocks. Then, we will give a detailed introduction to the core component of LFMamba, the basic SSM block.

E. Basic SSM Block

As the fundamental component of LFMamba, the basic SSM block is responsible for effectively establishing long-range dependencies of each 2D LF slice as an alternative to Transformer block. As illustrated in Fig. 2(b). Following the design philosophy of Transformer, a two-stage structure is adopted in the basic SSM block. At the first stage, given an input 2D feature $F \in \mathbb{R}^{H \times W \times C}$ (batch dimension is omitted), we employ a LayerNorm (LN) operation followed by our proposed efficient S6 block to establish long-range dependencies of each pixel, and we adopt learnable skip connection with scale factor $s_1 \in \mathbb{R}^C$ between the input and the output

$$\bar{F} = S6(LN(F)) + s_1 \cdot F, \quad (9)$$

Then, in the second stage, after normalizing \bar{F} by LayerNorm, following [47], we employ a convolution (Conv) layer to capture local details followed by a channel attention (CA) layer to enhance the channel interaction. At last, we also utilize a learnable scale factor s_2 on residual learning in this stage.

$$\hat{F} = CA(Conv(LN(\bar{F})) + s_2 \cdot \bar{F}) \quad (10)$$

Efficient S6. The vanilla Mamba was initially introduced for casual modeling of 1D sequences, which poses significant

challenges when adapting to non-causal data such as images [43]. To solve this problem, plenty of vision mambas have proposed various multi-direction 2D scanning strategies to alleviate directional sensitiveness, such as bidirectional scan [42], cross-scan [43], continuous-scan [49], and etc. Inspired by [43], we introduce the efficient S6 block for efficient and effective handling of 2D LF informative slices

As illustrated in Fig. 2(c), the efficient S6 block follows the design paradigm of the Visual State-Space (VSS) block introduced in [43] which employs a two-stream structure. Despite the strong modeling capability presented by [43], we surprisingly find that directly utilizing the original SS2D in VSS block [43] achieves sub-optimal results compared to existing leading methods with more parameters. Improving the performance by simply adding more layers or expanding the channel dimension will result in a larger model size and longer execution time which is unsatisfactory. To this end, we propose a novel efficient SS2D (ESS2D) mechanism that is integrated into the efficient S6 block. Therefore, given an input feature $\mathbf{F} \in \mathbb{R}^{H \times W \times C}$, the whole process of efficient S6 can be described as

$$\begin{aligned} \mathbf{F}_1 &= \text{LN}(\text{ESS2D}(\text{SiLU}(\text{DWConv}(\text{Linear}(\mathbf{F}))))), \\ \mathbf{F}_2 &= \text{SiLU}(\text{Linear}(\mathbf{F})), \\ \hat{\mathbf{F}} &= \text{Linear}(\mathbf{F}_1 \odot \mathbf{F}_2) \end{aligned} \quad (11)$$

where SiLU denotes the sigmoid-weighted linear unit activation function [59], DWConv denotes the depth-wise convolution, and \odot represents the Hadamard product.

As illustrated in Fig. 3, the upper subplot shows the original SS2D proposed in [43]. To facilitate modeling non-causal 2D images, SS2D duplicates the input feature four times, and each copy will be flattened into a 1D sequence in different orders for long-term dependency learning. Finally, the output can be obtained by adding them together. In contrast, ESS2D divides the input data into four groups along the channel dimension, then each data group is flattened into a 1D sequence in four directions for further feature extraction. Eventually, each data sequence is restored to the original 2D data and concatenate back together. This simple alternation brings considerable declines of parameters, which mainly occurs on the two linear projection layers in Fig. 2(c) while sacrificing little learning ability. This allows us to ultimately cascade two basic SSM blocks in Spatial/Angular/EPI-H/V SSM blocks to enhance the modeling capability further.

Notably, our proposed ESS2D is similar to the Parallel Vision Mamba Layer (PVM) in [57] but has some major differences. At first, the PVM also divides the input data into four groups along channel dimension, but the scan order for these four parts is the same. Second, the PVM is a multi-branch structure equipped with four parallel Mamba blocks, the Mamba block corresponds to our proposed efficient S6 block, which means that the division operation of the input in [57] happens before feeding into the Mamba block, while ours happens inside the efficient S6 block. Please refer to [57] for more detailed introduction of PVM.

F. Algorithm of LFMamba for LFSR

In summary, the detailed algorithm for achieving super-resolution of light field images using LFMamba is shown in Algorithm 1.

Algorithm 1 LFMamba for LFSR

Input: Low resolution light field image \mathcal{L}_{lr}
Output: High resolution light field image \mathcal{L}_{hr}

- 1: # Step 1: Project \mathcal{L}_{lr} to embedding space
- 2: $\mathbf{F}_{init} = H_{IFE}(\mathcal{L}_{lr})$ ▷ IFE module
- 3: # Step 2: Extract spatial and angular information
- 4: Let $\mathbf{F}^0 = \mathbf{F}_{init}$
- 5: **for** $i = 1, 2, 3$ **do**
- 6: $\mathbf{F}^i = H_{spa}^i(H_{ang}^i(\mathbf{F}^{i-1}))$ ▷ SAFL module
- 7: **end for**
- 8: $\mathbf{F}_{sa} = \mathbf{F}_{init} + \mathbf{F}^2$
- 9: # Step 3: Extract structure information
- 10: Let $\mathbf{F}^0 = \mathbf{F}_{sa}$
- 11: **for** $i = 1, 2, 3$ **do**
- 12: $\mathbf{F}^i = H_{epi-h}^i(H_{epi-v}^i(\mathbf{F}^{i-1}))$ ▷ LSFL module
- 13: **end for**
- 14: $\mathbf{F}_{struct} = \mathbf{F}_{sa} + \mathbf{F}^2$
- 15: # Step 4: Generate \mathbf{F}_{fuse} using Eq. (6)
- 16: $\mathbf{F}_{fuse} = H_{fuse}(\mathbf{F}_{init}, \mathbf{F}_{sa}, \mathbf{F}_{struct})$
- 17: # Step 5: Generate \mathcal{L}_{hr} ▷ HLFR module
- 18: $\mathcal{L}_{hr} = H_{HLFR}(\mathbf{F}_{fuse})$

IV. EXPERIMENT

A. Dataset and Implementation Details

Following prior works [16, 18], we select five LFSR benchmarks (i.e., EPFL [61], HCIOld [62], HCInew [63], INRIA [64], STFGantry [65]) for training and evaluation. More specifically, we use the central 5×5 sub-aperture images from the original LFs and crop them into 32×32 and 64×64 patches for $2 \times$ and $4 \times$ SR, followed by bicubic downsampling to generate low-resolution 16×16 patches. Data augmentation is conducted by random 90-degree rotation and flipping in horizontal and vertical directions. We select L_1 loss as our loss function, and Adam as our optimizer with $\beta_1 = 0.9$ and $\beta_2 = 0.999$. The initial learning rate is set to 2×10^{-4} and will be halved every 15 epochs in total 60 epochs. The batch size is set to 2 for training. All the experiments are conducted on one PC with an RTX 2080 Ti GPU.

B. Comparison to state-of-the-art

We compare our method with fifteen state-of-the-art methods, including one single image SR method [60], ten CNN-based LF image SR methods [12–21] and four Transformer-based LF image SR methods [31, 32, 35, 36]. We use PSNR and SSIM as quantitative metrics to evaluate the performance. For one dataset with M scenes, we first get the average metric of $U \times V$ SAIs of each scene, then we obtain the metric of this dataset by averaging over M scenes.

Quantitative Results. Table I presents the quantitative comparisons between our method and other state-of-the-art

TABLE I
 QUANTITATIVE COMPARISON (PSNR / SSIM) OF DIFFERENT METHODS FOR $\times 2$ AND $\times 4$ SR. THE BEST AND THE SECOND BEST RESULTS ARE MARKED WITH RED AND BLUE COLORS. THE PARAMETERS (#PARAM.) AND FLOPS ARE CALCULATED ON AN INPUT LIGHT FIELD WITH SIZE $5 \times 5 \times 32 \times 32$.

Method	Scale	#Param.(M)	FLOPs(G)	EPFL	HCnew	HCold	INRIA	STFgantry	Average
Bicubic	$\times 2$	-	-	29.50/9350	31.69/9335	37.46/9776	31.10/9563	30.82/9473	31.11/9542
RCAN [60]	$\times 2$	15.3	389.75	33.16/9635	34.98/9602	41.05/9875	35.01/9769	36.33/9825	36.11/9742
resLF [12]	$\times 2$	7.98	37.06	32.75/9672	36.07/9715	42.61/9922	34.57/9784	36.89/9873	36.58/9793
LFSSR [13]	$\times 2$	0.88	25.70	33.69/9748	36.86/9753	43.75/9939	35.27/9834	38.07/9902	37.73/9835
LF-InterNet [17]	$\times 2$	5.04	47.46	34.14/9761	37.28/9769	44.45/9945	35.80/9846	38.72/9916	38.08/9847
LF-ATO [14]	$\times 2$	1.22	597.66	34.27/9757	37.24/9767	44.20/9942	36.15/9842	39.64/9929	38.15/9843
MEG-Net [15]	$\times 2$	1.69	48.40	34.34/9773	37.42/9777	44.08/9942	36.09/9849	38.77/9915	38.14/9851
LF-DFNet [16]	$\times 2$	3.94	57.22	34.44/9766	37.44/9786	44.23/9943	36.36/9841	39.61/9935	38.41/9854
IINet [19]	$\times 2$	4.84	56.16	34.68/9773	37.74/9790	44.84/9948	36.57/9853	39.86/9936	38.74/9857
LF-SAV [20]	$\times 2$	1.22	34.65	34.62/9772	37.43/9776	44.22/9942	36.36/9849	38.69/9914	38.26/9851
DistgSSR [18]	$\times 2$	3.53	64.11	34.81/9787	37.96/9796	44.94/9949	36.59/9859	40.40/9942	38.94/9866
HLFSR [21]	$\times 2$	13.72	167.40	35.31/9800	38.32/9807	44.98/9950	37.06/9867	40.85/9947	39.30/9874
DPT [31]	$\times 2$	3.73	65.34	34.48/9758	37.35/9771	44.31/9943	36.40/9843	39.52/9926	38.40/9848
LFT [32]	$\times 2$	1.11	56.16	34.80/9781	37.84/9791	44.52/9945	36.59/9855	40.51/9941	38.85/9863
EPIT [36]	$\times 2$	1.42	69.71	34.83/9775	38.23/9810	45.08/9949	36.67/9853	42.17/9957	39.40/9877
LF-DET [35]	$\times 2$	1.59	48.50	35.26/9797	38.31/9807	44.99/9950	36.95/9864	41.76/9955	39.45/9875
LFMamba	$\times 2$	2.15	62.95	35.75/9824	38.36/9810	44.98/9950	37.07/9876	40.95/9948	39.42/9882
LFMamba †	$\times 2$	2.15	62.95	35.84/9832	38.59/9816	45.20/9952	37.19/9880	41.15/9950	39.59/9886
Bicubic	$\times 4$	-	-	25.14/8311	27.61/8507	32.42/9335	26.82/8860	25.93/8431	27.58/8701
RCAN [60]	$\times 4$	15.4	391.25	27.88/8863	29.63/8886	35.20/9548	29.76/9276	28.90/9131	30.27/9141
resLF [12]	$\times 4$	8.64	39.70	28.27/9035	30.73/9107	36.71/9682	30.34/9412	30.19/9372	31.25/9322
LFSSR [13]	$\times 4$	1.77	128.44	28.27/9118	30.72/9145	36.70/9696	30.31/9467	30.15/9426	31.23/9370
LF-InterNet [17]	$\times 4$	5.48	50.10	28.67/9162	30.98/9161	37.11/9716	30.64/9491	30.53/9409	31.58/9388
LF-ATO [14]	$\times 4$	1.36	686.99	28.52/9115	30.88/9135	37.00/9699	30.71/9484	30.61/9430	31.54/9373
MEG-Net [15]	$\times 4$	1.77	102.20	28.74/9160	31.10/9177	37.28/9716	30.66/9490	30.77/9453	31.71/9399
LF-DFNet [16]	$\times 4$	3.99	57.31	28.77/9165	31.23/9196	37.32/9718	30.83/9503	31.15/9494	31.86/9415
IINet [19]	$\times 4$	4.88	57.42	29.11/9188	31.36/9208	37.62/9734	31.08/9515	31.21/9502	32.08/9429
LF-SAV [20]	$\times 4$	1.54	115.80	29.37/9223	31.45/9217	37.50/9721	31.27/9531	31.36/9505	32.19/9439
DistgSSR [18]	$\times 4$	3.58	65.41	28.99/9195	31.38/9217	37.56/9732	30.99/9519	31.65/9535	32.11/9440
HLFSR [21]	$\times 4$	13.87	182.52	29.20/9222	31.57/9238	37.78/9742	31.24/9534	31.64/9537	32.29/9455
DPT [31]	$\times 4$	3.78	66.55	28.93/9170	31.19/9188	37.39/9721	30.96/9503	31.14/9488	31.92/9414
LFT [32]	$\times 4$	1.16	57.60	29.25/9210	31.46/9218	37.63/9735	31.20/9524	31.86/9548	32.28/9447
EPIT [36]	$\times 4$	1.47	74.96	29.34/9197	31.51/9231	37.68/9737	31.37/9526	32.18/9571	32.40/9452
LF-DET [35]	$\times 4$	1.69	51.20	29.47/9230	31.56/9235	37.84/9744	31.39/9534	32.14/9573	32.48/9463
LFMamba	$\times 4$	2.30	66.90	29.84/9256	31.70/9249	37.91/9748	31.81/9551	31.85/9554	32.62/9472
LFMamba †	$\times 4$	2.30	66.90	29.95/9275	31.86/9265	38.08/9755	31.90/9563	32.04/9568	32.77/9485

Notes: † denotes geometry assembling strategy.

methods. LFMamba achieves competitive results across five datasets for both $\times 2$ and $\times 4$ SR while maintaining a moderate model size. Overall, LFMamba performs closely to LF-DET [35] on $\times 2$ SR with only 0.03dB lower average PSNR but a 0.0007 higher average SSIM. While for the more challenging $\times 4$ SR, LFMamba surpasses LF-DET by an average of 0.14dB in PSNR and 0.0009 in SSIM. Particularly noteworthy are LFMamba’s remarkable performance gains on real-world LF datasets EPFL and INRIA, which exhibit more intricate structures. This underscores LFMamba’s capability to explore the intrinsic structure of LF effectively. However, it’s also worth noting that LFMamba’s performance on datasets with large disparities is somewhat unstable. For instance, while it outperforms LF-DET by 0.14dB in $\times 4$ SR on HCnew dataset (disparity range: [-4, 4]), it lags behind LF-DET and EPIT on the STFgantry dataset (disparity range: [-7, 7]) by 0.29dB and 0.33dB respectively. To address this imbalance, we employ a geometry assembling strategy to further enhance overall performance and narrow the performance gap on the STFgantry dataset between LFMamba, EPIT, and LF-DET, which brings an average PSNR increase of 0.17dB for $\times 2$ and 0.15dB for $\times 4$ SR, respectively.

Qualitative Results. We also present qualitative results achieved by different methods on more challenging $\times 4$ SR task. As depicted in Fig. 4, LFMamba excels in recovering sharp edges and intricate textures, a feat that eludes most competing methods. For instance, in the scene *ISO_Chart_1* from the EPFL dataset, many methods struggle to reconstruct the horizontal lines between figures ‘2’ and ‘3’, whereas LFMamba accomplishes this task effectively. In the scene *Red_&White_Building* from the EPFL dataset, we can observe that only our LFMamba can reconstruct clear and complete diagonal red line of the no-parking marker. In the scene *Origami* from HCnew dataset, LFMamba successfully recovers the spots and lines on the red jar, indicating the efficacy of LFMamba.

Computational Efficiency. To evaluate the computational efficiency of LFMamba, we compare the model parameters, FLOPs, memory consumption, and inference time of different state-of-the-art models on $\times 4$ SR task. For parameters and FLOPs, we can see that from Table. I, compared to the leading three CNN-based methods, i.e., IINet [19], DistgSSR [18], and HLFSR [21], our LFMamba has fewer parameters or FLOPs while achieving better performance. Compared

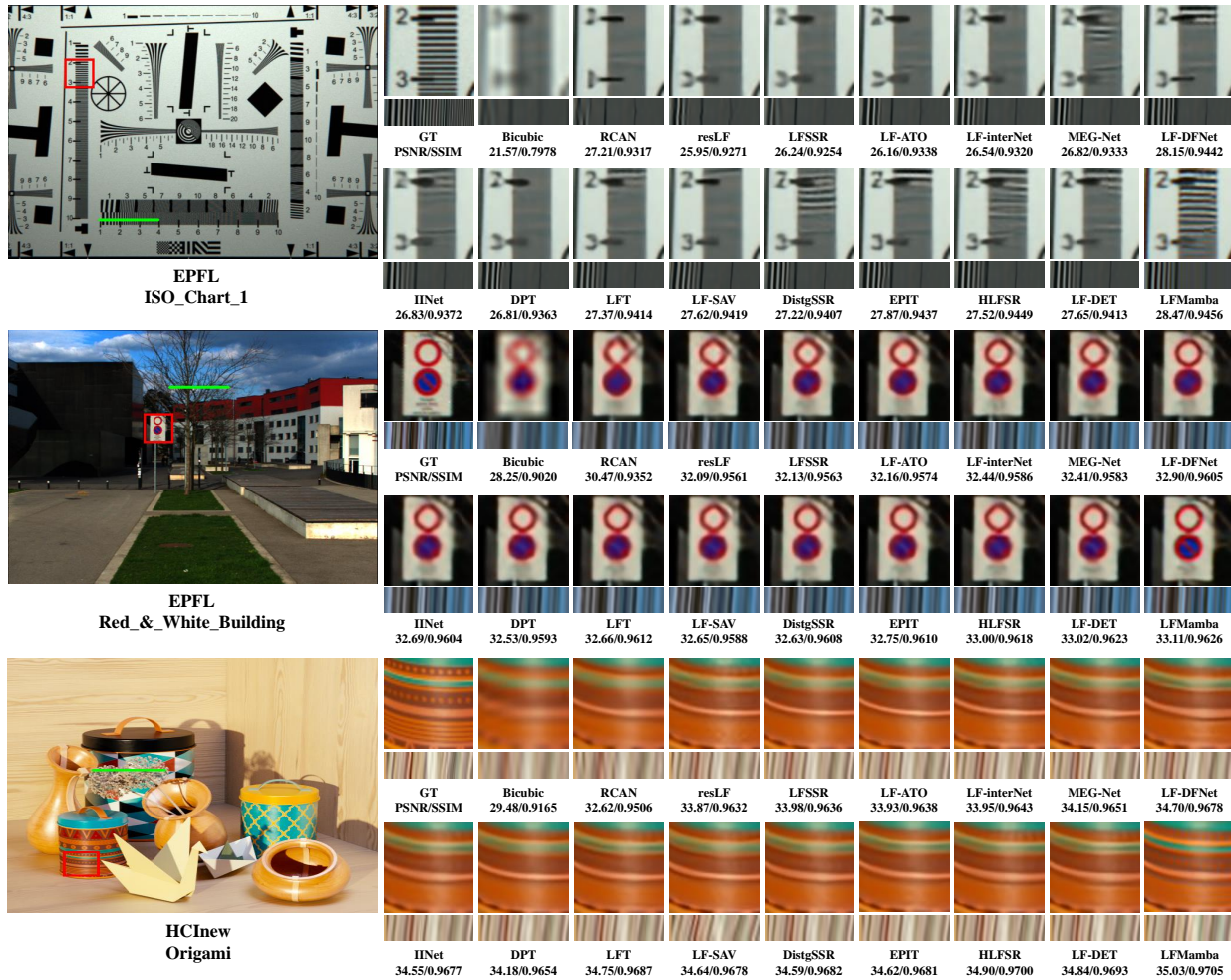


Fig. 4. Visual comparisons of different methods for $4\times$ LFSR. The first column shows the HR central view image and the rest columns present: 1) the close-ups of the super-resolved images by different methods, 2) the epipolar plane images, and 3) the PSNR and SSIM. Best viewed zoom-in.

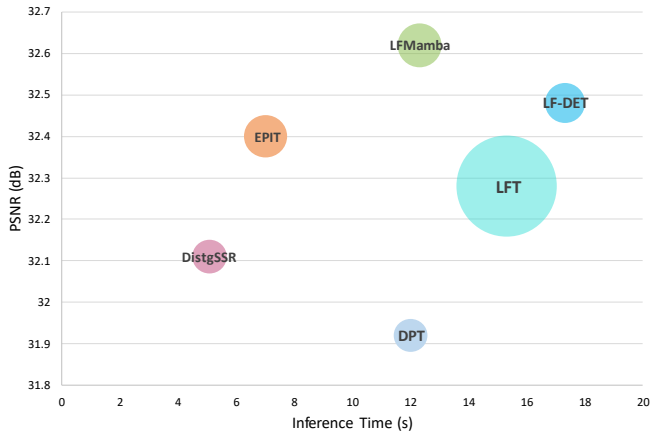


Fig. 5. Computational efficiency comparison between LFMamba and SOTA methods on $4\times$ SR. The area of circles denotes the memory consumption. The inference time is calculated by averaging the inference time of all scenes across the five test datasets.

to Transformer-based methods, our LFMamba also keeps a moderate model size although LFMamba has more network layers, which is attributed to our proposed efficient S6 block.

Regarding inference time and memory consumption, we evaluate these metrics by averaging the inference time across 23 scenes from five test datasets and measuring peak memory usage on the GPU. Since convolution operation is inherently more efficient than self-attention calculation due to the computational complexity and modern GPU acceleration algorithms. We select one CNN-based method, DistgSSR [18] as the baseline model, and other Transformer-based methods and our LFMamba for comparison. The results are shown in Fig. 5, our LFMamba obtains a good balance on performance and efficiency. In general, LFMamba’s inference time is faster than LFT and LF-DET and is comparable to DPT. However, there is still a gap between LFMamba and EPIT as EPIT adopts self-attention on EPis, which have a smaller feature size, and EPIT only has ten Transformer layers while our LFMamba has 24 SSM layers. Additionally, LFMamba consumes acceptable memory footprints (reflected by the circle size), indicating that it can effectively super-resolve LF images with limited resources. Note that, all model inferences are conducted in the same environment using an Nvidia 2080Ti GPU.

C. Ablation Study

LF Structure Feature Learning. As previously discussed,

TABLE II

ABLATION STUDIES OF LFMAMBA. THE FIRST THREE ROWS INVESTIGATE THE EFFECT OF LF STRUCTURE LEARNING. THE SECOND THREE ROWS COMPARES THE EFFECTIVENESS OF MAMBA AND TRANSFORMER. THE THIRD TWO ROWS INVESTIGATE THE MULTI-LEVEL FEATURE FUSION STRATEGIES.

Model variants	#Params.(M)	EPFL	Δ	HCInew	Δ	HCInold	Δ	INRIA	Δ	STFgantry	Δ
<i>LFMamba</i>	2.30	29.84	-	31.70	-	37.91	-	31.81	-	31.85	-
<i>w/o EPI</i>	2.39	29.57	-0.27	31.68	-0.02	37.79	-0.12	31.46	-0.35	32.01	+0.16
<i>w/ 3D</i>	2.23	29.63	-0.21	31.60	-0.10	37.76	-0.15	31.59	-0.22	32.09	+0.24
<i>w/ reverse</i>	2.30	29.58	-0.26	31.58	-0.12	37.74	-0.17	31.45	-0.36	31.75	-0.10
<i>w/ LFT</i>	1.65	29.70	-0.14	31.66	-0.04	37.87	-0.04	31.68	-0.13	31.92	+0.07
<i>w/ EPIT</i>	2.34	29.63	-0.21	31.69	-0.01	37.88	-0.03	31.55	-0.26	32.23	+0.38
<i>w/ LFT_EPIT</i>	2.26	29.59	-0.25	31.62	-0.08	37.94	+0.03	31.57	-0.24	32.21	+0.36
<i>w/o fusion</i>	2.17	29.63	-0.21	31.65	-0.05	37.90	-0.01	31.72	-0.09	32.01	+0.16
<i>w sum</i>	2.17	29.64	-0.20	31.70	-	37.85	-0.05	31.65	-0.16	31.92	+0.07

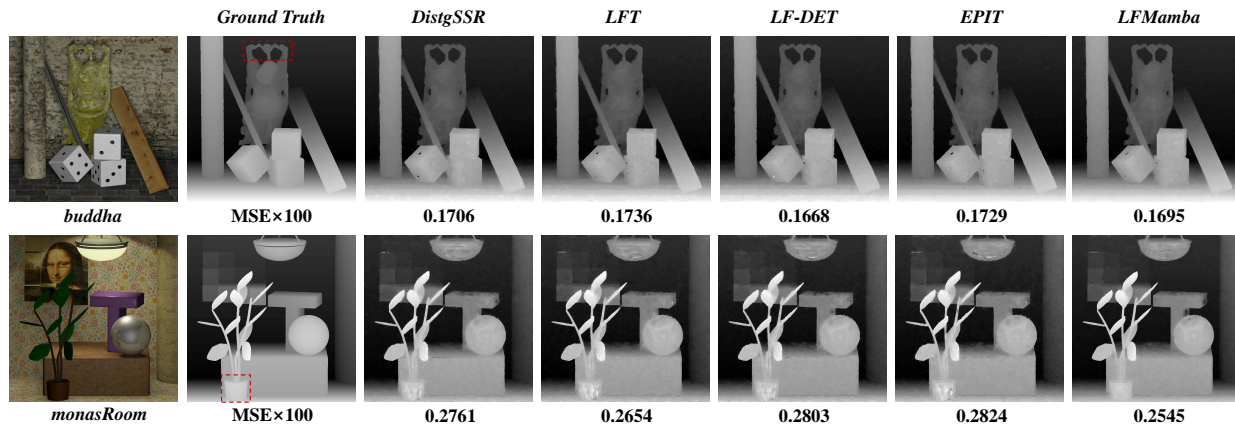


Fig. 6. Depth estimation results achieved by SPO [66] using $\times 4$ SR LF images generated by different LFSR methods. The mean square error multiplied by 100 ($MSE \times 100$) is chosen as the quantitative metric.

the structural characteristics of LFs is indispensable for reconstructing HR LF images. To probe the efficacy of our proposed LFMamba, we develop three model variants. **First**, we remove all the EPI-H/V SSM blocks and build a model with five spatial-angular SSM blocks, denoted as '*w/o EPI*' to illustrate the necessity of LF structure learning. **Second**, we achieve LF structure learning through learning the relationships of bi-directional sub-aperture image sequences as introduced in Fig. 1 **Mid**, denoted as '*w/ 3D*'. **Last**, we invert the order of spatial-angular feature learning and LF structure learning, denoted as '*w/ reverse*' to investigate the impact of the learning orders of spatial-angular information and LF structure.

From the first three rows in Tabel II, we can conclude that. First, the absence of LF structure learning leads to a performance drop on most datasets, especially for real-world datasets (i.e., EPFL, INRIA). Second, learning LF structure information from 3D image sequence perspective benefits the exploration of the STFgantry dataset, while is sub-optimal in other datasets. Because when the disparity is small, spatial and angular information contribute more to recovering fine-grained details. Third, extracting spatial-angular information is privileged, indicating that the effectiveness of LF structure learning can be maximized after spatial-angular feature learning.

Mamba vs. Transformer. We develop three model variants '*w/ LFT*', '*w/ EPIT*', and '*w/ LFT_EPIT*' to investigate the performance comparison between Mamba and Transformer. Specifically, '*w/ LFT*' means we replace the spatial and

angular SSM with the spatial and angular Transformer in LFT [32]. '*w/ EPIT*' means we substitute the EPI-V/H SSM with the non-local Transformer block proposed in EPIT [36]. And '*w/ LFT_EPIT*' denotes both happens. From the middle three rows in Table. II, we observe that, using Transforms on spatial and angular leads to an overall performance drop except for STFgantry with minor improvements. The integration of non-local Transformer block brings significant robustness to the STFgantry dataset, but also can not avoid performance drops on other datasets.

Multi-level Feature Fusion Strategies. We explore the impact of multi-level features (i.e., F_{init} , F_{sa} , and F_{struct}) usage by introduce two model variants. **First**, we don't use feature fusion, denoted as '*w/o fusion*'. This leads to an overall performance decline while surprisingly benefiting the STFgantry dataset, indicating that the utilization of multi-level features promotes the exploration of inherent LF information. **Second**, we replace the concatenation operation with the element summation operation, which we find even worse than the results of '*w/o fusion*', demonstrating the effectiveness of our multi-level feature fusion strategy.

Numbers of the basic SSM block. We further explore the impact of the numbers of basic SSM block in spatial/angular/EPI-H/V SSM blocks. As shown in Table. III, on $\times 4$ SR task, when we utilize one basic SSM block, the model already reaches EPIT's [36] performance on average PSNR with the same parameters but lower FLOPs. However,

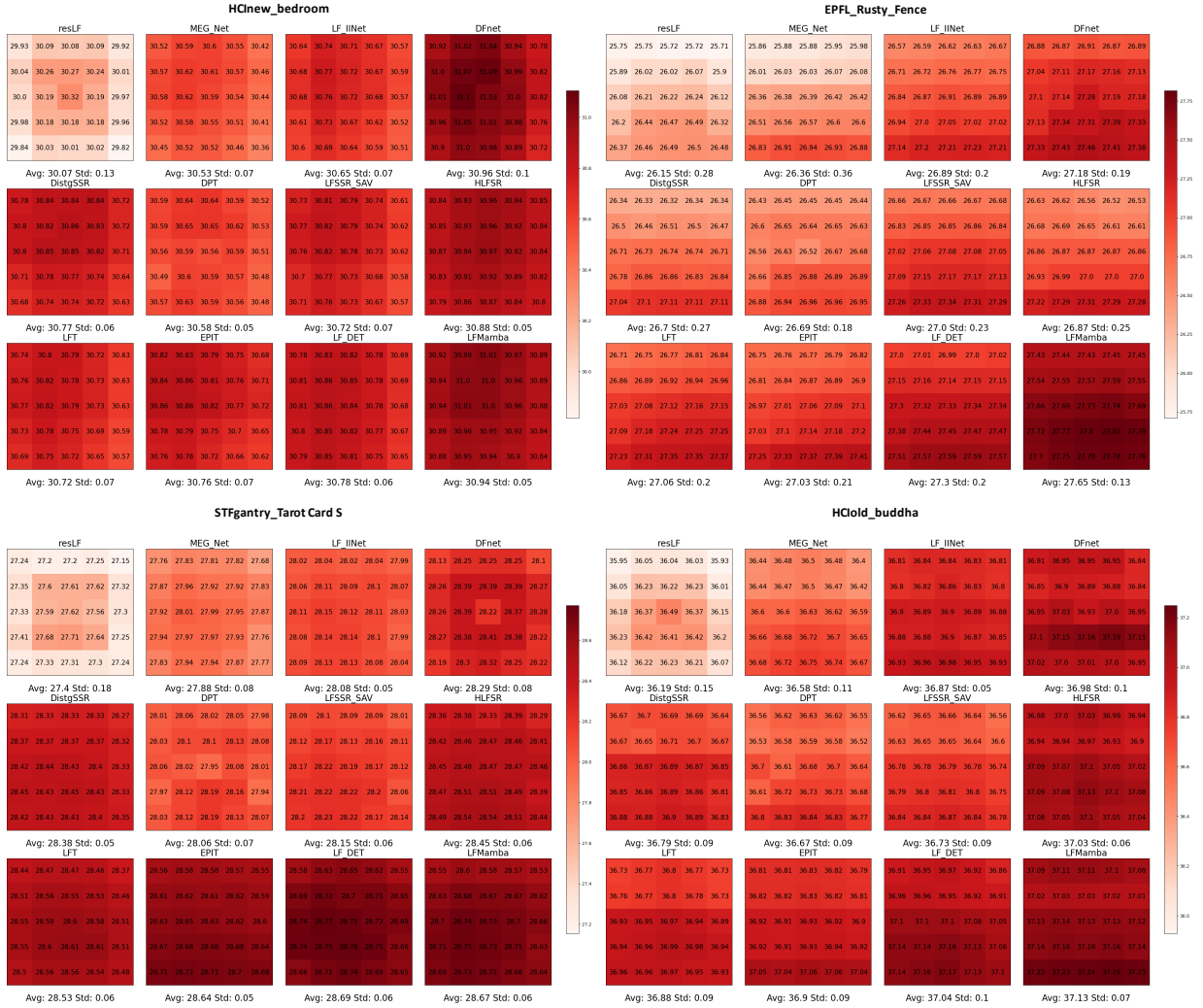


Fig. 7. **Visualization of the PSNR distributions w.r.t. perspectives.** We also present the average PSNR and standard deviation for each method, lower standard deviation represents higher angular consistency.

TABLE III
ABLATION STUDIES OF THE NUMBERS OF BASIC SSM BLOCK ON $\times 4$ SR.

Nums.	#Params.(M)	FLOPs(G)	Average PSNR
1	1.47	43.17	32.40
2 (LFMamba)	2.30	66.90	32.62
3	3.13	90.64	32.57

employing three basic SSM blocks fails to bring consistent improvements. Therefore, we ultimately use two basic SSM blocks in LFMamba.

D. Angular Consistency

We also investigate the angular consistency of different models from the following three perspectives. **First**, we measure the angular consistency through the fidelity of the reconstructed EPIs. As shown in Fig. 4, for instance, in the scene *ISO_Chart_1* from the EPFL dataset, the left part of the EPIs reconstructed by all the other methods present aliased results, while ours result is smoother which benefited from the LF structure learning. **Second**, we measure the angular con-

sistency by using the $4\times$ SR results for depth estimation using the SPO [66] algorithm. We select *buddha* and *monasRoom* from HCIold datasets with ground truth depth map as test objectives and use mean square error as the quantitative metric. As shown in Fig. 6, our LFMamba achieves the best score on the scene *monasRoom* and the second score on *buddha*, which represents high angular consistency. **Last**, we evaluate the angular consistency by comparing the PSNR distributions of all views on some representative scenes for $4\times$ SR. As shown in Fig. 7, our LFMamba can achieve superior performance while obtaining a low standard deviation, showcasing that LFMamba can reconstruct high-quality HR LF images across all angular views, demonstrating its high angular consistency.

E. LFMamba for LF Angular SR

To investigate the generalization ability of our proposed method, we apply our proposed LFMamba for LF angular SR (LFASR) task by simply modifying the HR LF Reconstruction module and remaining the rest part unchanged. Concretely, we take $2\times 2 \rightarrow 7\times 7$ LFASR task as an example, after getting the deep fused feature (i.e., $F_{fuse} \in \mathbb{R}^{2\times 2\times H\times W\times C}$),

TABLE IV
 QUANTITATIVE COMPARISON (PSNR/SSIM) BETWEEN DIFFERENT METHODS IN 2×2 TO 7×7 ANGULAR SR TASK. THE BEST RESULTS ARE BOLDDED, AND THE SECOND BEST ARE UNDERLINED

Method	#Params.(M)	HCold	HCInew	Average
DistgASR [18]	2.68	42.18/0.978	34.70/0.974	38.44/ 0.976
EASR-L [67]	6.63	41.54/0.971	35.86/0.975	<u>38.70/0.973</u>
LFMamba-ASR	2.23	<u>42.03/0.975</u>	<u>35.61/0.977</u>	38.82/0.976

a 2×2 convolution without padding is performed on the angular dimension the generate an angular sparse-downsampled feature $F_s \in \mathbb{R}^{1 \times 1 \times H \times W \times C}$. Then, a 1×1 convolution is applied to expand the channel followed by pixel-shuffle to generate angular dense-sampled feature $F_d \in \mathbb{R}^{7 \times 7 \times H \times W \times C}$. Finally, a 3×3 convolution is used to produce the final output $\mathcal{L} \in \mathbb{R}^{7 \times 7 \times H \times W}$.

Following [18, 67], we select two datasets HCold [62] and HCInew [63] for experiments. We choose the central 7×7 SAIs as high angular resolution LFs and crop them into 64×64 patches, and its corner 2×2 SAIs as low angular resolution input LFs. During training LFMamba-ASR, we select L_1 loss and use Adam as the optimizer with $\beta_1 = 0.9$ and $\beta_2 = 0.999$. The initial learning rate is set to 2×10^{-4} and will be halved every 15 epochs in total 60 epochs and the batch size is set to 2. Data augmentation is also conducted as the same as LFMamba.

We compare LFMamba-ASR with two state-of-the-art methods DistgASR [18] and EASR-L [67], both are CNN-based networks. The quantitative results are shown in Table. IV, although LFMamba-ASR ranks second place both in HCold and HCInew dataset, it achieves the best average PSNR/SSIM score across these two datasets with the smallest model size. The qualitative results are shown in Fig. 8, we select two challenging scenes *dishes* from HCInew and *stillLife* from HCold for comparisons. The reconstructed central view SAIs by LFMamba-ASR present fewer artifacts in the letter area of *dishes* and fabric area of *stillLife*. From the error maps, we can observe that LFMamba-ASR can reconstruct more accurate images. The promising results on LFASR demonstrate our proposed method’s effectiveness and generalization abilities for utilizing SSM to learn LF features.

V. LIMITATIONS AND FUTURE WORK

Although LFMamba presents its competitive capability compared to existing leading LFSR methods, it still exhibits some limitations and can be further improved with more careful designs. For instance, as a pure SSM-based network, LFMamba is adept at recovering the sharp edges and fine-grained textures when the disparity is relatively small while encountering obstacles when the disparity is getting large. The experimental results indicate that a more robust retrofit on the basic SSM block or a combination of SSM and Transformer is worth trying. Additionally, since this work mainly focuses on the scanning approach to LFs, broader consideration of the exploration of other priors such as frequency analysis of LFs could be taken in future studies.

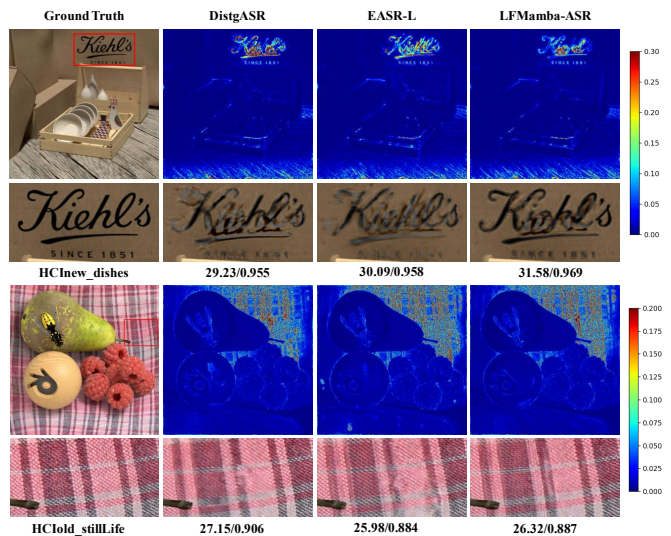


Fig. 8. Visual results of the reconstructed central view image achieved by different methods. We also present the error map between the results and ground truth.

VI. CONCLUSION

In this work, we integrate the recent advanced Selective State Space Model, i.e., Mamba into Light Field image Super-Resolution (LFSR). We start with analyzing the probable approaches and ultimately choosing to employ Mamba on LFs’ informative 2D slices to comprehensively explore the spatial contextual information, complementary angular information, and LF structure information. Based on that, we propose LFMamba, a pure SSM-based network built upon our proposed efficient SS2D mechanism, which facilitates efficient and effective exploration of the rich LF information. Extensive experiments demonstrate the competitiveness in terms of performance and efficiency of LFMamba against state-of-the-art CNN- and Transformer-based LFSR methods. We further explore the generalization ability of our method by applying LFMamba for LFASR task and achieving promising results, further demonstrating that our proposed method can effectively learn inherent LF features from a representation learning perspective.

REFERENCES

- [1] T.-C. Wang, A. A. Efros, and R. Ramamoorthi, “Occlusion-aware depth estimation using light-field cameras,” in *Proceedings of the IEEE international conference on computer vision*, 2015, pp. 3487–3495.
- [2] Y. Wang, J. Yang, Y. Guo, C. Xiao, and W. An, “Selective light field refocusing for camera arrays using bokeh rendering and superresolution,” *IEEE Signal Processing Letters*, vol. 26, no. 1, pp. 204–208, 2018.
- [3] N. Li, J. Ye, Y. Ji, H. Ling, and J. Yu, “Saliency detection on light field,” in *Proceedings of the IEEE conference on computer vision and pattern recognition*, 2014, pp. 2806–2813.
- [4] Y. Yoon, H.-G. Jeon, D. Yoo, J.-Y. Lee, and I. S. Kweon, “Light-field image super-resolution using convolutional neural network,” *IEEE Signal Processing Letters*, vol. 24, no. 6, pp. 848–852, 2017.

- [5] C. Dong, C. C. Loy, K. He, and X. Tang, "Image super-resolution using deep convolutional networks," *IEEE transactions on pattern analysis and machine intelligence*, vol. 38, no. 2, pp. 295–307, 2015.
- [6] Z. Yu, J. Yu, A. Lumsdaine, and T. Georgiev, "An analysis of color demosaicing in plenoptic cameras," in *2012 IEEE Conference on Computer Vision and Pattern Recognition*. IEEE, 2012, pp. 901–908.
- [7] T. E. Bishop and P. Favaro, "The light field camera: Extended depth of field, aliasing, and superresolution," *IEEE transactions on pattern analysis and machine intelligence*, vol. 34, no. 5, pp. 972–986, 2011.
- [8] M. Alain and A. Smolic, "Light field super-resolution via lfbm5d sparse coding," in *2018 25th IEEE international conference on image processing (ICIP)*. IEEE, 2018, pp. 2501–2505.
- [9] K. Mitra and A. Veeraraghavan, "Light field denoising, light field superresolution and stereo camera based refocussing using a gmm light field patch prior," in *2012 IEEE Computer Society Conference on Computer Vision and Pattern Recognition Workshops*. IEEE, 2012, pp. 22–28.
- [10] M. Rossi and P. Frossard, "Geometry-consistent light field super-resolution via graph-based regularization," *IEEE Transactions on Image Processing*, vol. 27, no. 9, pp. 4207–4218, 2018.
- [11] Y. Wang, F. Liu, K. Zhang, G. Hou, Z. Sun, and T. Tan, "Lfnnet: A novel bidirectional recurrent convolutional neural network for light-field image super-resolution," *IEEE Transactions on Image Processing*, vol. 27, no. 9, pp. 4274–4286, 2018.
- [12] S. Zhang, Y. Lin, and H. Sheng, "Residual networks for light field image super-resolution," in *Proceedings of the IEEE/CVF conference on computer vision and pattern recognition*, 2019, pp. 11 046–11 055.
- [13] H. W. F. Yeung, J. Hou, X. Chen, J. Chen, Z. Chen, and Y. Y. Chung, "Light field spatial super-resolution using deep efficient spatial-angular separable convolution," *IEEE Transactions on Image Processing*, vol. 28, no. 5, pp. 2319–2330, 2018.
- [14] J. Jin, J. Hou, J. Chen, and S. Kwong, "Light field spatial super-resolution via deep combinatorial geometry embedding and structural consistency regularization," in *Proceedings of the IEEE/CVF conference on computer vision and pattern recognition*, 2020, pp. 2260–2269.
- [15] S. Zhang, S. Chang, and Y. Lin, "End-to-end light field spatial super-resolution network using multiple epipolar geometry," *IEEE Transactions on Image Processing*, vol. 30, pp. 5956–5968, 2021.
- [16] Y. Wang, J. Yang, L. Wang, X. Ying, T. Wu, W. An, and Y. Guo, "Light field image super-resolution using deformable convolution," *IEEE Transactions on Image Processing*, vol. 30, pp. 1057–1071, 2020.
- [17] Y. Wang, L. Wang, J. Yang, W. An, J. Yu, and Y. Guo, "Spatial-angular interaction for light field image super-resolution," in *Computer Vision—ECCV 2020: 16th European Conference, Glasgow, UK, August 23–28, 2020, Proceedings, Part XXIII 16*. Springer, 2020, pp. 290–308.
- [18] Y. Wang, L. Wang, G. Wu, J. Yang, W. An, J. Yu, and Y. Guo, "Disentangling light fields for super-resolution and disparity estimation," *IEEE Transactions on Pattern Analysis and Machine Intelligence*, vol. 45, no. 1, pp. 425–443, 2022.
- [19] G. Liu, H. Yue, J. Wu, and J. Yang, "Intra-inter view interaction network for light field image super-resolution," *IEEE Transactions on Multimedia*, vol. 25, pp. 256–266, 2021.
- [20] Z. Cheng, Y. Liu, and Z. Xiong, "Spatial-angular versatile convolution for light field reconstruction," *IEEE Transactions on Computational Imaging*, vol. 8, pp. 1131–1144, 2022.
- [21] V. Van Duong, T. N. Huu, J. Yim, and B. Jeon, "Light field image super-resolution network via joint spatial-angular and epipolar information," *IEEE Transactions on Computational Imaging*, vol. 9, pp. 350–366, 2023.
- [22] A. Vaswani, N. Shazeer, N. Parmar, J. Uszkoreit, L. Jones, A. N. Gomez, Ł. Kaiser, and I. Polosukhin, "Attention is all you need," *Advances in neural information processing systems*, vol. 30, 2017.
- [23] A. Dosovitskiy, L. Beyer, A. Kolesnikov, D. Weissenborn, X. Zhai, T. Unterthiner, M. Dehghani, M. Minderer, G. Heigold, S. Gelly, J. Uszkoreit, and N. Houlsby, "An image is worth 16x16 words: Transformers for image recognition at scale," in *International Conference on Learning Representations*, 2021.
- [24] Z. Liu, Y. Lin, Y. Cao, H. Hu, Y. Wei, Z. Zhang, S. Lin, and B. Guo, "Swin transformer: Hierarchical vision transformer using shifted windows," in *Proceedings of the IEEE/CVF international conference on computer vision*, 2021, pp. 10 012–10 022.
- [25] N. Carion, F. Massa, G. Synnaeve, N. Usunier, A. Kirillov, and S. Zagoruyko, "End-to-end object detection with transformers," in *European conference on computer vision*. Springer, 2020, pp. 213–229.
- [26] Z. Sun, S. Cao, Y. Yang, and K. M. Kitani, "Rethinking transformer-based set prediction for object detection," in *Proceedings of the IEEE/CVF international conference on computer vision*, 2021, pp. 3611–3620.
- [27] S. Zheng, J. Lu, H. Zhao, X. Zhu, Z. Luo, Y. Wang, Y. Fu, J. Feng, T. Xiang, P. H. Torr *et al.*, "Rethinking semantic segmentation from a sequence-to-sequence perspective with transformers," in *Proceedings of the IEEE/CVF conference on computer vision and pattern recognition*, 2021, pp. 6881–6890.
- [28] R. Strudel, R. Garcia, I. Laptev, and C. Schmid, "Segmnet: Transformer for semantic segmentation," in *Proceedings of the IEEE/CVF international conference on computer vision*, 2021, pp. 7262–7272.
- [29] J. Liang, J. Cao, G. Sun, K. Zhang, L. Van Gool, and R. Timofte, "Swinir: Image restoration using swin transformer," in *Proceedings of the IEEE/CVF international conference on computer vision*, 2021, pp. 1833–1844.
- [30] S. W. Zamir, A. Arora, S. Khan, M. Hayat, F. S. Khan, and M.-H. Yang, "Restormer: Efficient transformer for high-resolution image restoration," in *Proceedings of the IEEE/CVF conference on computer vision and pattern recognition*, 2022, pp. 5728–5739.
- [31] S. Wang, T. Zhou, Y. Lu, and H. Di, "Detail-preserving transformer for light field image super-resolution," in *Proceedings of the AAAI conference on artificial intelligence*, vol. 36, no. 3, 2022, pp. 2522–2530.
- [32] Z. Liang, Y. Wang, L. Wang, J. Yang, and S. Zhou, "Light field image super-resolution with transformers," *IEEE Signal Processing Letters*, vol. 29, pp. 563–567, 2022.
- [33] Y. Wang, Y. Lu, S. Wang, W. Zhang, and Z. Wang, "Local-global feature aggregation for light field image super-resolution," in *ICASSP 2022-2022 IEEE International Conference on Acoustics, Speech and Signal Processing (ICASSP)*. IEEE, 2022, pp. 2160–2164.
- [34] Z. Wang and Y. Lu, "Multi-granularity aggregation transformer for light field image super-resolution," in *2022 IEEE International Conference on Image Processing (ICIP)*. IEEE, 2022, pp. 261–265.
- [35] R. Cong, H. Sheng, D. Yang, Z. Cui, and R. Chen, "Exploiting spatial and angular correlations with deep efficient transformers for light field image super-resolution," *IEEE Transactions on Multimedia*, 2023.
- [36] Z. Liang, Y. Wang, L. Wang, J. Yang, S. Zhou, and Y. Guo, "Learning non-local spatial-angular correlation for light field image super-resolution," in *Proceedings of the IEEE/CVF International Conference on Computer Vision*, 2023, pp. 12 376–12 386.
- [37] A. Gu, K. Goel, and C. Re, "Efficiently modeling long sequences with structured state spaces," in *International Conference on Learning Representations*, 2022.
- [38] J. T. Smith, A. Warrington, and S. Linderman, "Simplified state space layers for sequence modeling," in *The Eleventh*

- International Conference on Learning Representations*, 2023.
- [39] A. Gu, I. Johnson, K. Goel, K. Saab, T. Dao, A. Rudra, and C. Ré, “Combining recurrent, convolutional, and continuous-time models with linear state space layers,” *Advances in neural information processing systems*, vol. 34, pp. 572–585, 2021.
- [40] D. Y. Fu, T. Dao, K. K. Saab, A. W. Thomas, A. Rudra, and C. Re, “Hungry hungry hippos: Towards language modeling with state space models,” in *The Eleventh International Conference on Learning Representations*, 2023.
- [41] A. Gu and T. Dao, “Mamba: Linear-time sequence modeling with selective state spaces,” *arXiv preprint arXiv:2312.00752*, 2023.
- [42] L. Zhu, B. Liao, Q. Zhang, X. Wang, W. Liu, and X. Wang, “Vision mamba: Efficient visual representation learning with bidirectional state space model,” *arXiv preprint arXiv:2401.09417*, 2024.
- [43] Y. Liu, Y. Tian, Y. Zhao, H. Yu, L. Xie, Y. Wang, Q. Ye, and Y. Liu, “Vmamba: Visual state space model,” *arXiv preprint arXiv:2401.10166*, 2024.
- [44] J. Ma, F. Li, and B. Wang, “U-mamba: Enhancing long-range dependency for biomedical image segmentation,” *arXiv preprint arXiv:2401.04722*, 2024.
- [45] Y. Yang, Z. Xing, and L. Zhu, “Vivim: a video vision mamba for medical video object segmentation,” *arXiv preprint arXiv:2401.14168*, 2024.
- [46] R. Deng and T. Gu, “Cu-mamba: Selective state space models with channel learning for image restoration,” *arXiv preprint arXiv:2404.11778*, 2024.
- [47] H. Guo, J. Li, T. Dai, Z. Ouyang, X. Ren, and S.-T. Xia, “Mambair: A simple baseline for image restoration with state-space model,” *arXiv preprint arXiv:2402.15648*, 2024.
- [48] Y. Shi, B. Xia, X. Jin, X. Wang, T. Zhao, X. Xia, X. Xiao, and W. Yang, “Vmambair: Visual state space model for image restoration,” *arXiv preprint arXiv:2403.11423*, 2024.
- [49] C. Yang, Z. Chen, M. Espinosa, L. Ericsson, Z. Wang, J. Liu, and E. J. Crowley, “Plainmamba: Improving non-hierarchical mamba in visual recognition,” *arXiv preprint arXiv:2403.17695*, 2024.
- [50] Y. Yuan, Z. Cao, and L. Su, “Light-field image superresolution using a combined deep cnn based on epi,” *IEEE Signal Processing Letters*, vol. 25, no. 9, pp. 1359–1363, 2018.
- [51] B. Lim, S. Son, H. Kim, S. Nah, and K. Mu Lee, “Enhanced deep residual networks for single image super-resolution,” in *Proceedings of the IEEE conference on computer vision and pattern recognition workshops*, 2017, pp. 136–144.
- [52] W. Wang, E. Xie, X. Li, D.-P. Fan, K. Song, D. Liang, T. Lu, P. Luo, and L. Shao, “Pyramid vision transformer: A versatile backbone for dense prediction without convolutions,” in *Proceedings of the IEEE/CVF international conference on computer vision*, 2021, pp. 568–578.
- [53] Z. Shen, M. Zhang, H. Zhao, S. Yi, and H. Li, “Efficient attention: Attention with linear complexities,” in *Proceedings of the IEEE/CVF winter conference on applications of computer vision*, 2021, pp. 3531–3539.
- [54] T. Dao, D. Fu, S. Ermon, A. Rudra, and C. Ré, “Flashattention: Fast and memory-efficient exact attention with io-awareness,” *Advances in Neural Information Processing Systems*, vol. 35, pp. 16 344–16 359, 2022.
- [55] H. Mehta, A. Gupta, A. Cutkosky, and B. Neyshabur, “Long range language modeling via gated state spaces,” in *The Eleventh International Conference on Learning Representations*, 2023.
- [56] E. Nguyen, K. Goel, A. Gu, G. Downs, P. Shah, T. Dao, S. Baccus, and C. Ré, “S4nd: Modeling images and videos as multidimensional signals with state spaces,” *Advances in neural information processing systems*, vol. 35, pp. 2846–2861, 2022.
- [57] R. Wu, Y. Liu, P. Liang, and Q. Chang, “Ultralight vm-unet: Parallel vision mamba significantly reduces parameters for skin lesion segmentation,” *arXiv preprint arXiv:2403.20035*, 2024.
- [58] M. Levoy and P. Hanrahan, “Light field rendering,” in *Seminal Graphics Papers: Pushing the Boundaries, Volume 2*, 2023, pp. 441–452.
- [59] S. Elfving, E. Uchibe, and K. Doya, “Sigmoid-weighted linear units for neural network function approximation in reinforcement learning,” *Neural networks*, vol. 107, pp. 3–11, 2018.
- [60] Y. Zhang, K. Li, K. Li, L. Wang, B. Zhong, and Y. Fu, “Image super-resolution using very deep residual channel attention networks,” in *Proceedings of the European conference on computer vision (ECCV)*, 2018, pp. 286–301.
- [61] M. Rerabek and T. Ebrahimi, “New light field image dataset,” in *8th International Conference on Quality of Multimedia Experience (QoMEX)*, 2016.
- [62] S. Wanner, S. Meister, and B. Goldluecke, “Datasets and benchmarks for densely sampled 4d light fields,” in *VMV*, vol. 13, 2013, pp. 225–226.
- [63] K. Honauer, O. Johannsen, D. Kondermann, and B. Goldluecke, “A dataset and evaluation methodology for depth estimation on 4d light fields,” in *Computer Vision-ACCV 2016: 13th Asian Conference on Computer Vision, Taipei, Taiwan, November 20-24, 2016, Revised Selected Papers, Part III 13*. Springer, 2017, pp. 19–34.
- [64] M. Le Pendu, X. Jiang, and C. Guillemot, “Light field inpainting propagation via low rank matrix completion,” *IEEE Transactions on Image Processing*, vol. 27, no. 4, pp. 1981–1993, 2018.
- [65] V. Vaish and A. Adams, “The (new) stanford light field archive,” *Computer Graphics Laboratory, Stanford University*, vol. 6, no. 7, 2008.
- [66] S. Zhang, H. Sheng, C. Li, J. Zhang, and Z. Xiong, “Robust depth estimation for light field via spinning parallelogram operator,” *Computer Vision and Image Understanding*, vol. 145, pp. 148–159, 2016.
- [67] G. Liu, H. Yue, J. Wu, and J. Yang, “Efficient light field angular super-resolution with sub-aperture feature learning and macro-pixel upsampling,” *IEEE Transactions on Multimedia*, 2022.